

Article

Zircon U-Pb Ages and Geochemistry of the Granite in the Xintianling Tungsten Deposit, SE China: Implications for Geodynamic Settings of the Regional Tungsten Mineralization

Wu Yang, Min Zhang, Jun Yan and Xiaocui Chen *

Faculty of Resources and Environmental Engineering, Guizhou Institute of Technology, Guiyang 550003, China; yangwu@git.edu.cn (W.Y.); zhangmin@git.edu.cn (M.Z.); yanjun@git.edu.cn (J.Y.)

* Correspondence: chenxiaocui2007@163.com

Abstract: The Xintianling tungsten deposit is a super-large deposit in the Nanling tungsten–tin mineralization belt, which is genetically associated with the early-stage hornblende-biotite monzonitic granite of Qitianling pluton. The orebodies predominantly occur as veins and lenses within skarn rocks between Xintianling granite and limestone (Shidengzi group). In this work, whole-rock major and trace elements and zircon U–Pb ages of the Xintianling granite were studied in an attempt to investigate the geochronological framework, petrogenesis, tectonism, and metallogenesis with regard to the deposit. The petrographic and geochemical analyses indicated that the Xintianling granite consists of three intrusive units of medium- and coarse-grained biotite granite, fine-grained biotite granite, and granite porphyry, of which the biotite granite was strongly associated with mineralization. Biotite granite rocks are highly K-calc-alkaline and weakly peraluminous, with A/CNK ratios ranging from 0.99 to 1.05. Late-granite porphyry is aluminum-supersaturated with a high evolution degree, whose geochemical characteristics suggest that it is either an I- or S-type granite. LA-ICP-MS zircon U-Pb dating revealed that medium- and coarse-grained biotite granite (162.3 ± 1.2 Ma, MSWD = 1.3), fine-grained biotite granite (161.8 ± 1.3 Ma, MSWD = 1.8), and granite porphyry (154.3 ± 1.6 Ma, MSWD = 2.4) formed in the late Jurassic. The emplacement of the Qitianling A-type granite and associated tungsten-tin polymetallic mineralization is a continuous evolution process, and they are products of the large-scale mineralization of the Nanling in the middle–late Jurassic (150–160 Ma). Under the tectonic setting of the Mesozoic lithospheric extension, asthenosphere upwelling along deep-fault, intensive mantle–crust interaction processes probably provide not only the high heat flow, but also partly mantle-derived material for large-scale W-Sn-polymetallic mineralization in this area.

Keywords: zircon U-Pb; granite geochemistry; genesis; Xintianling tungsten deposit

Citation: Yang, W.; Zhang, M.; Yan, J.; Chen, X. Zircon U-Pb Ages and Geochemistry of the Granite in the Xintianling Tungsten Deposit, SE China: Implications for Geodynamic Settings of the Regional Tungsten Mineralization. *Minerals* **2022**, *12*, 952. <https://doi.org/10.3390/min12080952>

Academic Editor: Ryan Mathur

Received: 25 May 2022

Accepted: 26 July 2022

Published: 28 July 2022

Publisher's Note: MDPI stays neutral with regard to jurisdictional claims in published maps and institutional affiliations.



Copyright: © 2022 by the authors. Licensee MDPI, Basel, Switzerland. This article is an open access article distributed under the terms and conditions of the Creative Commons Attribution (CC BY) license (<https://creativecommons.org/licenses/by/4.0/>).

1. Introduction

The Nanling represents one of the most well-known, tungsten-rich areas in the world. The area is characterized by intensive magmatic activity. Previous geochronological studies have reported that, in this area, granite-related mineralization occurred from the Greenvillian to the late Yanshanian period, peaking during 150~160 Ma [1–3]. The Xintianling deposit was discovered over 20 years ago and has 330,000 tons of W_3O_8 , which is located in southern Hunan Province (e.g., the central part of the Nanling Range). Notably, it has always been acknowledged that Xintianling granite belongs to the Qitianling granite stock [4–8], but there are a limited number of studies regarding this granite. In particular, the petrogenetic and geodynamic backgrounds of the Nanling tungsten–tin metallogenic belt in the Mesozoic era remain controversial. The debate centers on two main points. The first school of thought proposes that granite in the belt is closely related to S-type granite, whereas the other thought is that the exposed granite is primarily A-type granite.

To clarify the above ambiguity, we focused on tungsten-related granite in the Xintianling deposit in south China. We first presented the major and trace element compositions

of the granite to clarify its genesis. Then, zircon U-Pb dating was conducted to place geochronologic constraints on intrusions and related mineralization. Our new results show that the Xintianling tungsten deposit was formed in the late Jurassic under a back-arc extensional setting. The events were likely triggered by the break-off or detachment of the flatly subducted Paleo-Pacific slab (Figure 1).

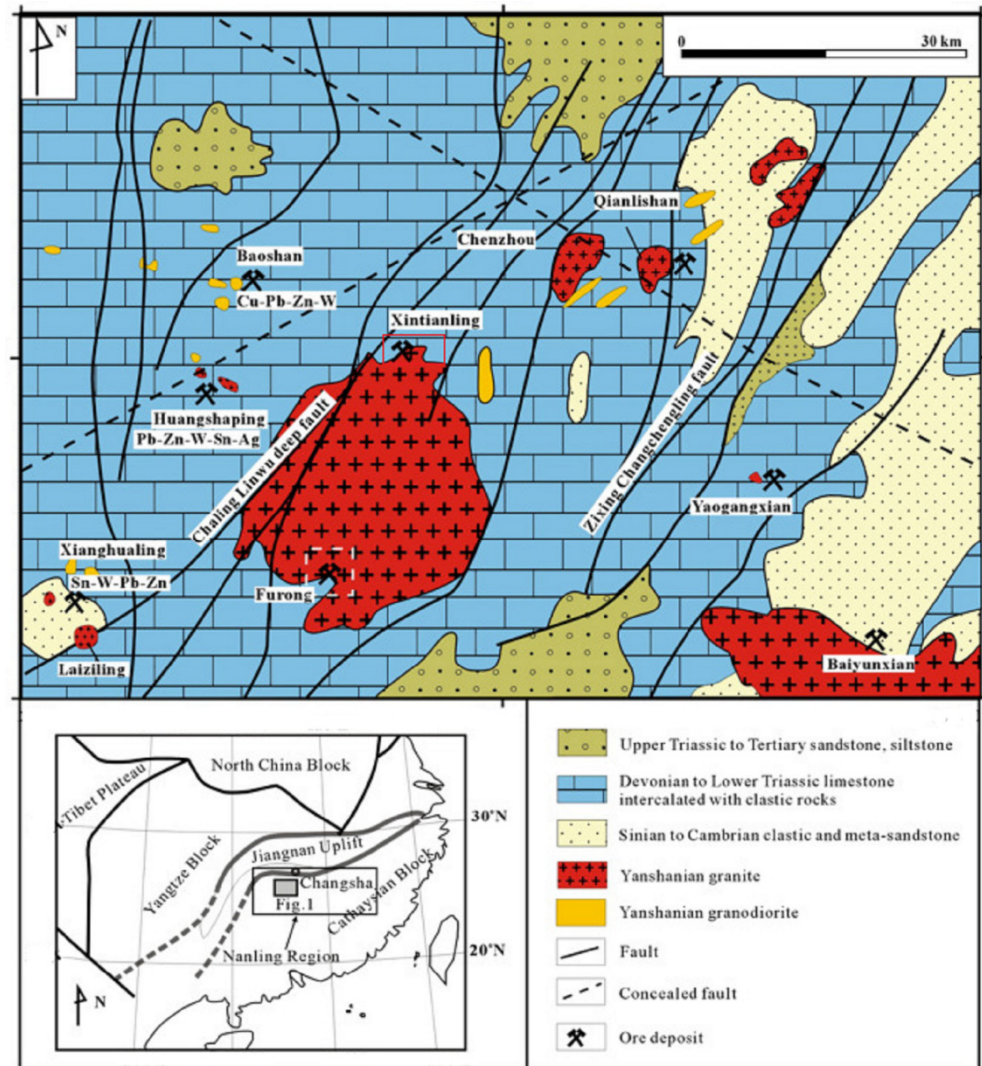


Figure 1. Simplified geological map of central Nanling region, South China, and distribution of mineral deposits in the region. (Peng et al. 2006) [5].

2. Regional Geological Characteristics

The Qianlishan–Qitianling research area has experienced many complicated tectonic movements at different stages and varying degrees, accompanied by magmatic activities. Its center is located where the Yangtze and the Cathaysian plates (the two major inland plates) converge and in the Chenzhou–Shaoyang strike-slip tectonomagmatic zone (Figure 2). The main area of the strike-slip tectonic zone lies within the Chenzhou–Shaoyang region, extending to the NW, to the Snowberg tectonic belt, but is outside Yaogangxian of Hunan Province in the southeast [9,10]. During that period, a significant ore-conducting structure developed in the area, controlling the distribution of ore fields with secondary structures controlling ore-body shapes and scales. The Yanling–Lanshan fault zone extends southwestward, from Yanling County to Langshan and through Chenzhou, with both ends stretching out through the province. It has a syndepositional foreland basin fault originating from the Sinian period (Early Paleozoic), a deep and large fault from the Caledonian movement

continuing until the Indo–Chinese–Yanshanian period, and a large-scale basement-cut fault with a long active period [11–14]. The Chenzhou–Shaoyang fault zone extends northwestward, from Yaogangxian through Chenzhou to Dayishan. It extends northwestward to the Snowberg arc structure belt at the center of Hunan and extends southeastward to Guangdong Indo–Chinese–Yanshanian in its important active period, causing the intrusion of intermediate-acid rocks from Guandimiao, Dayishan [14–18].

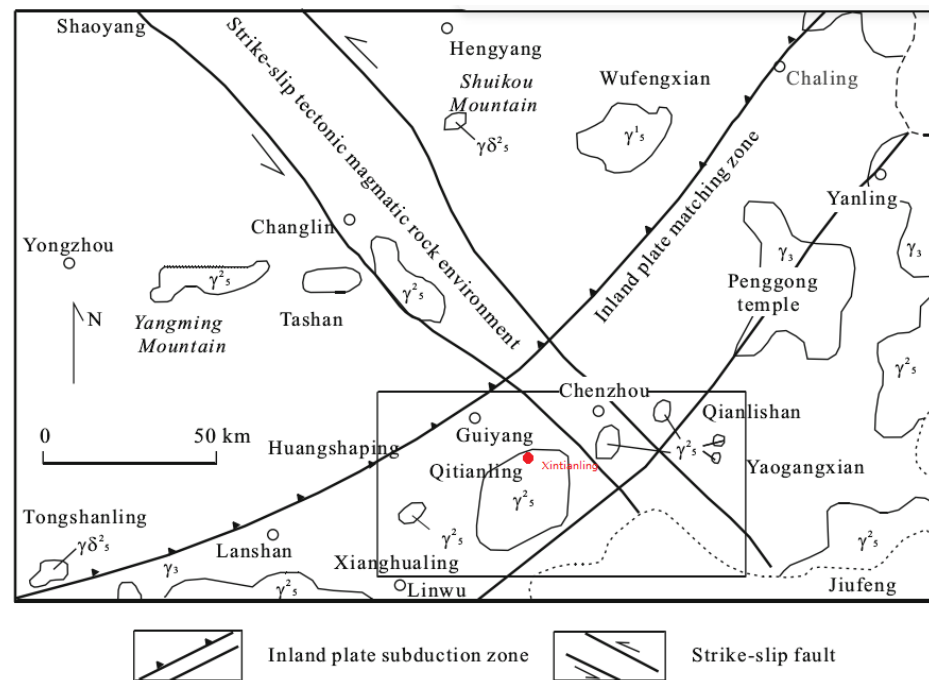


Figure 2. Tectonic setting of the Qianlishan–Qitianling area [7]. (γ_3 : Caledonian magmatic rock; γ^1_s : Indo–Chinese epoch magmatic rock; γ^2_s : Yanshanian magmatic rock; $\gamma\delta^2_s$: Yanshanian granodiorite).

3. Geologic Features of the Deposit

The Xintianling deposit is located north of the Qitianling pluton, which represents the central part of the Nanling Range. The strata are primarily carboniferous and covered locally by quaternary sediments. The carboniferous strata, from young to old, can be classified into the lower carboniferous YanGuan stage, the DaTang stage, and the middle–early Carboniferous TianHu stage. The exposed strata mainly consist of carbonates with silty and calcareous shale, and Permian carbonate rocks with ferromanganesian chert, siliceous and calcareous shale, which are unconformably overlain by Cretaceous red beds. Its mineralization is related to a north–south Duplex anticline. The main body of granite is micaceous granite, while the mineral grain size decreases from the center to the more peripheral zones of the pluton. It also can be divided into three lithologies: coarse-grained porphyritic biotite granite, medium- and coarse-grained porphyritic biotite granite, and fine- medium- and coarse-grained porphyritic biotite granite.

The main ore minerals present in the Xintianling deposit are scheelite and molybdenite, followed by small amounts of bismuthinite, galena, sphalerite, chalcopyrite, arsenopyrite, pyrrhotite, and pyrite. The main gangue minerals are garnet, diopside, actinolite, iron mica, chlorite, quartz, and small amounts of calcite, fluorite, epidote, etc. The main granular textures of the ores located here are automorphic, hypidiomorphic, and xenomorphic, as well as vein rocks. It should be noted that the main ore structures are disseminated structures. The main wall rock alterations that occur are skarnization silicification, greisenization, and marmorization. Notably, skarnization exhibits the most correlation with metallogenesis [19,20].

4. Sampling and Experimental Methods

The samples used in our study were collected from granite away from the mineralization in the Xintianling deposit. Petrographic observations (Figure 3) and chemical analysis (Table 1; see below) show that these samples suffered no hydrothermal alterations. We primarily selected two representative granites: medium- and coarse-grained porphyritic biotite granite and fine-grained biotite granite. Some granitic porphyries were tested in supplementary analyses (Figure 4).

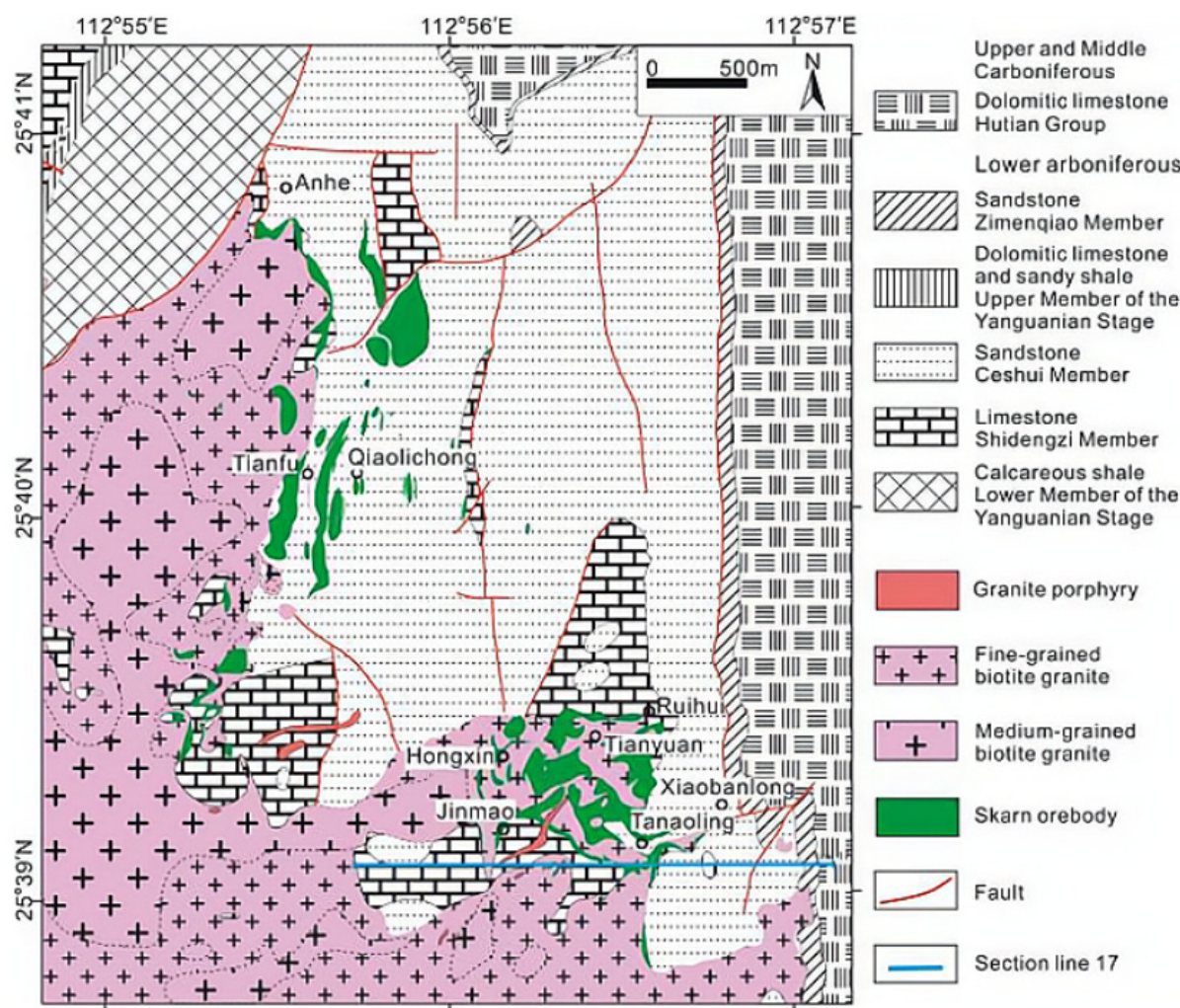


Figure 3. Sketch geological map of the Xintianling deposit (Zhang et al., 2015) [8].

Table 1. Main elements of granite in Xintianling ore field, Hunan (wt%).

SAMPLE		SiO ₂	Al ₂ O ₃	Fe ₂ O ₃	CaO	MgO	K ₂ O	Na ₂ O	TiO ₂	MnO	P ₂ O ₅	BaO	SrO	LOI
XTL-01	Medium-grained porphyritic biotite granite	70.1	14.25	3.19	2.29	0.8	4.66	2.95	0.45	0.06	0.18	0.11	0.03	0.72
XTL-07		66.1	15.4	4.54	2.66	1.18	4.34	3.34	0.65	0.09	0.27	0.1	0.04	1.12
XTL398		67.7	13.95	3.35	2.89	1.31	4.31	2.46	0.43	0.13	0.17	0.1	0.03	2.17
XTL-250-3		75.7	12.55	1.97	0.93	0.17	5.15	2.82	0.11	0.05	0.01	0.02	0.01	0.98
XTL-200-1		68.6	14.2	3.61	2.04	0.84	4.63	3.09	0.43	0.08	0.18	0.13	0.03	1.2
JY-468-3	Fine-grained biotite granite	72.4	12.75	2.28	1.82	0.53	5.54	2.03	0.23	0.06	0.09	0.05	0.02	2.18
AH-365-1-2		73.6	13.4	2.05	1.26	0.47	4.66	3.36	0.23	0.05	0.09	0.04	0.02	0.92
XTL-03		73.8	13	1.93	0.99	0.42	5.52	2.92	0.22	0.06	0.07	0.06	0.02	0.87
JY-415-01		74.9	13.05	1.14	1.23	0.19	4.61	3.44	0.11	0.07	0.02	0.02	0.01	0.88
AH-365-1-1		74.1	13.4	1.18	0.95	0.21	5.21	3.67	0.11	0.03	0.05	0.02	0.01	0.73
XT-160-3		76.3	12.45	0.98	1.09	0.08	4.32	3.59	0.06	0.03	0.01	0.02	0.01	0.93

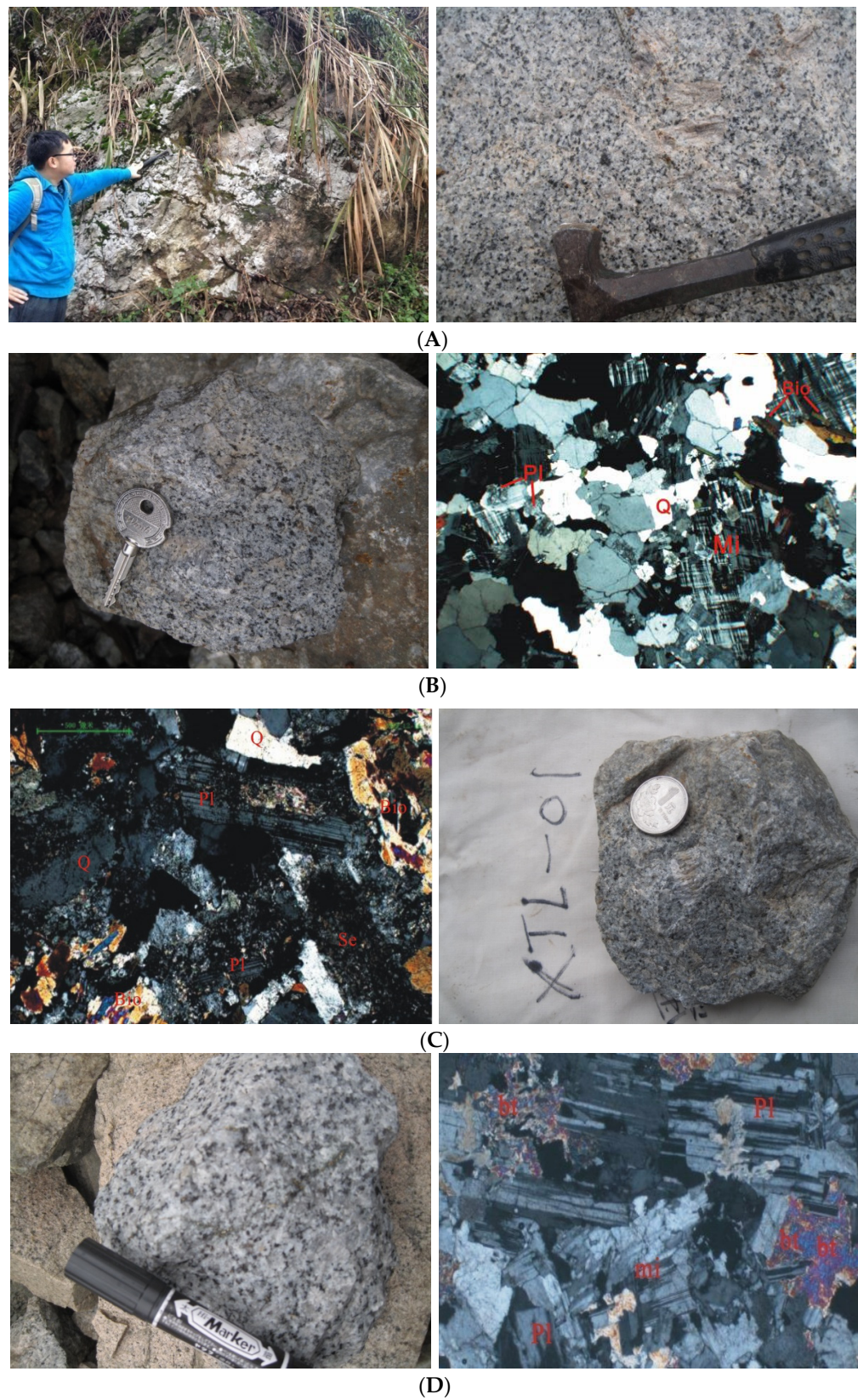


Figure 4. Field, macroscopic, and microscopic features of Xintianling granite. (A) Photos of granite outcrops in the wild; (B) Field hand specimen of granite porphyry and its microscopic characteristics (5×10 orthogonal polarized light); (C) Field hand specimen of granite porphyry and its microscopic characteristics (5×10 orthogonal polarized light); (D): Field hand specimens and microscopic features of pyritized biotite granite (5×10 orthogonal polarized light).

The major element abundances were determined using X-ray fluorescence, utilizing a Panalytical (formerly Philips Analytical Instruments Division) Model Axios (PW4400) spectrometer. The trace and rare-earth element abundances were analyzed via inductively coupled plasma mass spectrometry (ICP-MS) using a Finnigan MAT Model ELEMENT. The analyses were conducted in an ALS mineral laboratory in China. The detailed analytical procedures were previously described by Liu [4]. Two biotite granite samples (XTL-200-01-03 and XTL-340-7) and one granite porphyry sample (XTL-06) were selected for use in zircon dating. First, the fresh sample was crushed to a size of 200 meshes. Next, the zircon was selected under a binocular microscope. Target preparation and testing were subsequently performed based on this. The sample crushing, zircon selection, and target preparation were completed at the laboratory of Hebei Institute of Regional Geological and Mineral Survey, China. Analyses of zircon trace element contents and U-Pb isotope dating were simultaneously performed via LA-ICP-MS at the State Key Laboratory of Geological Processes and Mineral Resources, China University of Geosciences (Wuhan). The detailed instrument operating conditions and data-processing methods were identical to those used by Liu [4] and are briefly summarized below. We used the GeoLas 2005 laser ablation system, whereas the ICP-MS was conducted using Agilent 7500a. Helium and argon were used as the carrier and compensating gases, respectively, to adjust the sensitivity during the laser ablation process. The two gases were mixed via a T-joint before entering the ICP. A small amount of nitrogen was added to the plasma central gas flow (Ar + He) to enhance the instrument sensitivity, lower the detection limit, and increase the analytical precision. We calibrated the data with a standard sample during the test. Detailed instructions are given in the data analysis section.

5. Results

5.1. Geochemistry

After petrographic examination and the removal of altered surfaces, the samples for the whole-rock analysis were crushed in an agate mill to 200 mesh. X-ray fluorescence (XRF; Rigaku RIX 2100 spectrometer) using fused glass disks and ICP-MS (Agilent 7500a with a shield torch) was used to measure the major and trace-element compositions, respectively, of ALS Minerals (ALS Chemex) after the acid digestion of samples in Teflon bombs. The analytical precision was better than 5% for major elements and often better than 10% for trace elements [21]. The detailed analytical procedures for major-element analysis by XRF are described in [22], while those for trace element analysis by ICP-MS are described in [23].

The results of the analyses of major and trace elements are listed in Tables 1–5.

Table 2. Trace elements of granite in Xintianling ore field, Hunan (ppm).

SAMPLE		Rb	Cs	Ba	Hf	Th	U	Ta	Nb	W	Sr	Zr
XTL-01		269	13.65	951	6.1	27.1	9.34	2.9	24.8	2	306	205
XTL-07		224	10.65	922	8	39.9	8.77	2.6	27.8	2	416	289
XTL398	Medium-grained	282	31.7	865	5.9	24.3	6.72	1.6	21.1	14	282	212
XTL-250-03	porphyritic biotite	523	13.65	84.8	6.5	94.7	29.1	4.7	32.7	10	74.9	158
XTL-200-1	granite	215	7.49	1180	6.6	30.4	4.63	1.7	20.7	34	251	254
JY-468-3		291	18.45	394	4	33.9	16.8	1.5	22.6	30	141	140
AH-365-1-2		309	16.7	327	3.9	27.3	15.65	4.9	26.1	8	188	111
XTL-03		300	19.8	517	3.4	34.7	16.25	2.3	19.4	3	206	104
JY-415-01	Fine-grained biotite	404	51.5	84.3	3.3	29.1	28.1	3.3	24.4	18	81.1	72
AH-365-1-1	granite	427	14.7	163.5	3	19.65	23.5	11.3	45.9	9	106.5	53
XT-160-3		346	19.65	87	3.3	25.1	44.3	6.9	43.4	28	48.5	53

Table 3. Rare-earth element concentrations in granite in Xintianling ore field, Hunan (ppm).

SAMPLE		La	Ce	Pr	Nd	Sm	Eu	Gd	Tb	Dy	Ho	Er	Tm	Yb	Lu	Y
XTL-01	Medium-grained porphyritic biotite granite	57.9	113	12.15	41.5	7.76	1.4	5.98	0.87	4.49	0.83	2.32	0.36	2.3	0.33	24.8
XTL-07		95	181	18.95	61.9	11.4	1.79	8.35	1.17	5.88	1.13	3.1	0.47	2.75	0.47	33.2
XTL398		49.2	91.4	9.5	34.4	6.11	1.19	4.35	0.6	3.36	0.54	1.6	0.23	1.43	0.22	16.7
XTL-250-03		73.5	155	16.4	51.2	11.1	0.33	9.71	1.79	10.95	2.41	7.2	1.19	7.93	1.22	73.2
XTL-200-1		73	127.5	13.15	45.1	7.82	1.54	6.52	0.85	5.21	0.96	2.95	0.39	2.57	0.37	27.9
JY-468-3		29	50.5	5.03	16.7	2.85	0.59	2.47	0.37	2.25	0.43	1.44	0.22	1.45	0.26	16.3
AH-365-1-2		25.4	51.9	5.55	19.1	4.14	0.78	3.47	0.59	3.49	0.71	2.09	0.33	2.5	0.41	24.1
XTL-03	Fine-grained biotite granite	41.4	77.1	7.73	23.5	4.12	0.73	2.89	0.49	2.57	0.57	1.5	0.24	1.81	0.32	16.6
JY-415-01		12.3	26.2	3.03	12.3	3.04	0.49	2.89	0.44	2.69	0.58	2.1	0.27	2.27	0.41	19.1
AH-365-1-1		13.9	29.6	3.43	11.9	3	0.43	2.92	0.53	3.25	0.67	2	0.35	2.57	0.45	21.9
XT-160-3		6.9	17.8	2.43	10.9	3.84	0.49	4.28	0.79	5.51	1.12	3.75	0.55	3.93	0.64	31.7

Table 4. Rare-earth element characteristics in granite in Xintianling ore field, Hunan.

SAMPLE		ΣREE	LREE	HREE	w(LREE)/w(HREE)	LaN/YbN	δEu	δCe
XTL-01	Medium-grained porphyritic biotite granite	251.19	233.71	17.48	13.37	18.06	0.60	0.99
XTL-07		393.36	370.04	23.32	15.87	24.78	0.54	0.99
XTL398		204.13	191.80	12.33	15.56	24.68	0.67	0.97
XTL-250-03		349.93	307.53	42.40	7.25	6.65	0.09	1.05
XTL-200-1		287.93	268.11	19.82	13.53	20.37	0.64	0.93
JY-468-3		113.56	104.67	8.89	11.77	14.35	0.66	0.94
AH-365-1-2		120.46	106.87	13.59	7.86	7.29	0.61	1.02
XTL-03	Fine-grained biotite granite	164.97	154.58	10.39	14.88	16.41	0.61	0.98
JY-415-01		69.01	57.36	11.65	4.92	3.89	0.50	1.02
AH-365-1-1		75.00	62.26	12.74	4.89	3.88	0.44	1.02
XT-160-3		62.93	42.36	20.57	2.06	1.26	0.37	1.06

Table 5. CTPW standard minerals in granite in Xintianling ore field, Hunan, China.

Parameters\ Sample	XTL-01	XTL-03	XTL-07	XTL398	XTL-250-03	JY-415-01	XT-200-1	XTL-160-3	JY-468-3	AH-365-1-1	AH-365-1-2	AH-256-2
Quartz (Q)	31.67	34.4	23.26	31.6	37.17	34.78	28.56	37.16	37.1	30.91	33.02	5.78
Calcium feldspar (An)	10.54	4.66	11.93	13.89	4.62	6.09	9.47	5.43	8.73	4.5	5.84	0
Sodium feldspar (Ab)	21.09	22.8	27.76	17.8	23.88	29.07	25.14	29.83	14.51	31.07	28.49	44.34
Potash feldspar (Or)	27.71	32.9	26.04	26.24	30.63	27.58	27.99	25.79	33.39	31.13	27.79	1.77
Corundum (C)	1.3	0.94	1.1	1.01	0.68	0.28	1.04	0.06	0.86	0.16	0.75	0
Hypersthene (Hy)	3.39	1.89	5.02	5.28	1.5	1.1	3.89	0.74	2.52	1.03	2.11	13.37
Ilmenite (Il)	0.86	0.42	1.25	0.84	0.21	0.21	0.84	0.12	0.45	0.21	0.44	0.45
Magnetite (Mt)	1.92	1.24	2.72	1.93	1.24	0.72	2.21	0.62	1.4	0.78	1.28	0
Apatite (Ap)	0.42	0.16	0.64	0.41	0.02	0.05	0.43	0.02	0.21	0.12	0.21	0.12
Zircon (Zr)	0.04	0.02	0.06	0.04	0.03	0.01	0.05	0.01	0.03	0.01	0.02	0.02
Chromite (Cm)	0	0.01	0.01	0	0	0	0	0	0.01	0	0	0.01
Total	100.03	100.01	100.04	100.03	100.02	100	100.06	100.01	100.02	100.01	100	100.03
Differentiation index (DI)	80.47	90.1	77.06	75.64	91.68	91.43	81.69	92.78	85	93.11	89.3	51.89
Density g/cc	2.7	2.66	2.73	2.71	2.66	2.64	2.7	2.64	2.67	2.64	2.66	2.83
Liquid density	2.41	2.37	2.45	2.43	2.37	2.36	2.42	2.36	2.39	2.36	2.38	2.67
Dry viscosity	8.72	10.38	7.26	8.35	11.31	11.16	8.45	11.79	10.25	10.59	10.28	5.32
Wet viscosity	6.62	7.31	5.88	6.47	7.72	7.7	6.5	7.9	7.3	7.44	7.33	4.7
Liquidus temperature	839	767	902	853	734	740	846	717	778	757	769	1004
H ₂ O (%)	3.5	4.26	2.75	3.33	4.57	4.51	3.37	4.78	4.16	4.32	4.18	1.73
A/CNK	1.013	1.033	1.025	0.999	1.054	1.013	1.029	0.991	1.008	1	1.042	0.245
Consolidation index (SI)	7.01	3.93	8.99	11.67	1.7	2.04	7.02	0.9	5.17	2.06	4.51	1.63
Alkalinity rate (AR)	2.7	4.04	2.48	2.34	3.89	3.58	2.81	3.81	3.16	4.25	3.42	1.02
Composite indexσ43	2.13	2.31	2.52	1.82	1.94	2.02	2.3	1.87	1.93	2.53	2.09	0.01
Composite indexσ25	1.29	1.47	1.44	1.09	1.26	1.31	1.38	1.23	1.22	1.61	1.33	0

5.1.1. Major Elements

The results of the analysis of major elements are shown in Table 1. The SiO₂ content of the Xintianling granite varies from 66.1 wt% to 76.3 wt%, with an average of 72.11 wt%. The average SiO₂ content in medium- and coarse-grained porphyritic biotite granite is 70.6 wt%, whereas that of the fine-grained biotite granite is 74.78 wt%. Medium- and coarse-grained porphyritic biotite granite exhibits higher (MgO + CaO) contents with TFe > 1.00 wt% than fine-grained biotite granite. The K₂O and Na₂O contents in all the samples range from 4.31 wt% to 5.54 wt% and 2.03 wt% to 3.67 wt%, respectively (K₂O + Na₂O > 7.00%). It was found that K₂O/Na₂O is high (1.20–2.73). The Al₂O₃ contents are generally high in the samples, as they range from 12.45 wt% to 15.4 wt%, with an average of 13.49 wt%.

5.1.2. Trace Elements

The results of the analysis of trace elements are shown in Table 2. The mass fractions of large-ion lithophile elements (Rb, Cs, and Sr) were found to be stable. In most samples, the contents of Rb, Cs, and Sr varied from 215 to 346 ppm, 10.65 to 19.8 ppm, and 106.5 to 306 ppm, respectively. However, the large-ion lithophile element Ba exhibited a remarkable variability, fluctuating from 84.3 to 1180 ppm. The ratio of Sr/Ba was somewhat low, at 0.32–0.96. Moreover, non-active elements (Nb, Ta, Zr, and Hf) exhibit high contents, which vary within the ranges of 19.4–45.9 ppm, 1.5–11.3 ppm, 53–289 ppm, and 3–8 ppm, respectively. Notably, the Nb/Ta values range from 4.06 to 13.18. Xintianling granite is shown to be enriched with Rb, Sr, U, and other large-ion lithophile elements, while the levels of Nb, Th, and other high-field-strength elements are somewhat low.

5.1.3. REE

The results of the analysis of trace elements are shown in Table 3, while the statistical characteristics of the REEs are summarized in Table 4. As seen in Table 4, light REEs enriched granite at relatively high levels, as the LREE values range from 42.36 ppm to 370 ppm. It was found that the HREE values vary from 8.89 ppm to 42.4 ppm. At the same time, the LREE/HREE values are in the range of 2.06–15.87 and the ΣREE values vary from 69.93 ppm to 393 ppm, signifying low values. The δEu value is equal to 0.09–+0.67, the δCe value is 0.93–1.06, and the (La/Yb)_N value is higher in most samples (6.65–24.78). The rock mass CIPW calculation results are summarized in Table 5. As can be seen, the mass fractions of An, Ab, Or, Hy, Mt, and Zr vary within the ranges of 4.5–13.89, 14.51–29.07, 26.04–33.39, 0.74–5.28, and 0.62–2.72, respectively. The main rock-forming minerals are quartz, calcium feldspar, sodium feldspar, and orthoclase. Accessory minerals include corundum, hypersthene, magnetite, phosphorus pyroxene, zircon, chromite, etc. The mass fraction of the standard mineral corundum is generally low, i.e., it ranges between 0.16 and 1.3. Furthermore, it was found that the alkalinity rate is within the 2.34–4.25 range. Moreover, the solidification index was found to be between 0.9 and 11.67, with an average of 5. The aluminum saturation index was estimated to be within the 0.991–1.054 range, with a mean of 1.019 (<1.10). This finding demonstrates that rock belongs to the high K-Calc-alkaline (HKCA) series [24,25].

5.2. Zircon U-Pb Geochronology

Zircons were isolated from medium-grained porphyritic biotite granite and fine-grained biotite granite using combined magnetic and heavy liquid separation techniques at the Geological Laboratory of the Regional Geological Survey, Langfang City, Hebei Province, China. The zircon grains were examined under transmitted and reflected light using an optical microscope. Distinct domains within the zircons were selected for analysis based on their CL images. An Agilent 7500a ICP-MS equipped with a 193-nm laser was used. In the experiment, high-purity He was used as the carrier gas of the ablated substance. The laser operating frequency was 10 Hz, the laser spot diameter at the test point was 36 μm, and the effective acquisition time of the mass spectrometer was 45 s. U-Pb isotope fractionation uses the international standard zircon 91,500 as the external correction and

TEM (416 ± 5 Ma) and QH (160 ± 1 Ma) as monitoring standards. Samples housed at the State Key Laboratory of Geological Processes and Mineral Resources, China University of Geosciences (Wuhan), were used to measure the U–Pb ages of zircons. The ICP-MS DataCal (Ver. 6.7) [24] and Isoplot (Ver. 3.0) [25] programs were used for data reduction [26]. The correction for common Pb was performed following [27]. The dating results are presented in Tables 6–8.

Table 6. LA-ICPMS U–Pb zircon dating data of the XTL200 from the Xintianling deposit.

	Pb	Th	U	207Pb/206Pb	207Pb/206Pb	207Pb/235U	207Pb/235U	206Pb/238U	206Pb/238U	206Pb/238U	206Pb/238U
XTL-200-01	ppm	ppm	ppm	Ratio	1sigma	Ratio	1sigma	Ratio	1sigma	Age (Ma)	1sigma
1	35.19141	272.5146	839.0176	0.045944	0.000344	0.162493	0.01102	0.025865		164.6139	2.161754
2	73.76998	983.2053	668.4069	0.056646	0.003653	0.191286	0.011927	0.0254	0.000371	161.6922	2.330072
4	150.3792	1478.992	2434.117	0.053221	0.001753	0.189809	0.006196	0.025806	0.00026	164.248	1.636558
5	177.541	1613.307	3469.185	0.050773	0.001484	0.181493	0.005563	0.025795	0.000287	164.1755	1.804772
6	89.49963	948.6595	1368.104	0.053941	0.002318	0.195042	0.00915	0.025844	0.000324	164.4834	2.034622
9	48.18519	463.219	754.9348	0.056424	0.003868	0.201489	0.013901	0.025834	0.00037	164.4188	2.327648
10	262.391	3579.414	1976.90	0.050209	0.001792	0.181659	0.006409	0.026129	0.000263	166.2778	1.651446
11	53.20038	672.9266	595.3193	0.048573	0.003976	0.160214	0.012734	0.024771	0.000368	157.7413	2.31654
12	58.98816	537.3427	1241.274	0.048787	0.002503	0.163396	0.008134	0.024543	0.000279	156.3039	1.756469
13	120.7236	1294.406	1980.029	0.049217	0.001852	0.166427	0.006337	0.024362	0.000245	155.1676	1.540812
14	31.13808	305.9625	501.9875	0.052591	0.004471	0.176232	0.014161	0.025056	0.000422	159.5295	2.651531
15	42.34564	384.2241	605.2877	0.056603	0.003397	0.203768	0.011987	0.026479	0.000415	168.4726	2.608497
16	63.90019	833.8722	521.9321	0.050131	0.003748	0.173943	0.013597	0.025474	0.000384	162.1592	2.414481
17	135.3383	1800.57	860.6884	0.047541	0.003192	0.1716	0.011761	0.026629	0.00037	169.4154	2.3223
18	21.52203	277.3129	178.0327	0.047665	0.01037	0.146333	0.028933	0.024057	0.000702	153.2453	4.416119
Std-Qh-1	80.37841388	89.97414043	240.590879	0.074534707	0.002579302	1.839666506	0.060984163	0.179116608	0.002102619	161.146789	2.323197
Std-Qh-2	74.33384254	87.78273142	232.6301125	0.075225293	0.002667461	1.860733494	0.065194891	0.179223392	0.002212988	160.73057	1.295431
Std-Qh-3	82.54678906	91.79876654	248.9876897	0.068769	0.016213	0.213834	0.026246	0.038179	0.012715	160.4832123	1.292374
Std-Qh-4	79.86785431	88.90877652	230.3231234	0.059313	0.006757	0.204378	0.01679	0.028723	0.0003259	160.134521	1.139287

Table 7. LA-ICPMS U–Pb zircon dating data of the XTL06 from the Xintianling deposit.

	Pb	Th	U	207Pb/206Pb	207Pb/206Pb	207Pb/235U	207Pb/235U	206Pb/238U	206Pb/238U	206Pb/238U	206Pb/238U
XTL-06	ppm	ppm	ppm	Ratio	1sigma	Ratio	1sigma	Ratio	1sigma	Age (Ma)	1sigma
1	49.18345	474.7501	930.1068	0.05013	0.003061	0.163289	0.010028	0.023738	0.000309	151.2364	1.942938
4	32.88755	337.7602	601.4029	0.055275	0.004295	0.176264	0.012733	0.024043	0.000358	153.157	2.253025
5	118.9204	1275.754	2140.997	0.047771	0.001854	0.156585	0.00573	0.023865	0.000239	152.0385	1.505664
6	29.06759	305.5499	484.7007	0.054763	0.004053	0.17707	0.012689	0.024097	0.000374	153.4969	2.352972
7	50.5634	522.9461	939.0106	0.042862	0.002607	0.142702	0.008717	0.024115	0.000277	153.6105	1.744774
8	43.49626	420.021	866.6894	0.050735	0.003087	0.169779	0.00977	0.024627	0.000357	156.8348	2.243882
9	86.25562	705.0269	1877.608	0.05344	0.00213	0.181933	0.007077	0.024619	0.000253	156.7794	1.593041
10	87.45636	913.5775	1588.677	0.05087	0.002161	0.167509	0.006758	0.023973	0.000267	152.7182	1.677779
12	55.85148	556.9221	964.2869	0.051916	0.002559	0.175816	0.008175	0.024972	0.000336	159.0044	2.111661
13	24.13823	226.6071	445.012	0.053609	0.004565	0.184875	0.015556	0.025374	0.000403	161.529	2.533204
14	32.09021	267.1286	706.482	0.05031	0.003318	0.169702	0.010109	0.024982	0.000348	159.0658	2.188191
15	68.12095	661.1316	1358.808	0.048179	0.002254	0.159421	0.007021	0.024178	0.000275	154.0101	1.729854
16	46.29636	489.1592	875.4446	0.053796	0.002973	0.174047	0.00894	0.023738	0.000268	151.2355	1.688236
18	72.21149	668.9532	1304.427	0.05003	0.002163	0.165644	0.007092	0.024052	0.000269	153.2138	1.6907
Std-TEM	89.80875908	27.34027612	905.9055444	0.060127027	0.001658881	0.812591025	0.022311531	0.097591586	0.000757963	416.27543	2.898142235
Std-TEM	93.26105582	28.00151758	912.467429	0.062059732	0.001737264	0.836959751	0.02298062	0.097579211	0.000835196	417.98324	2.866857765
Std-TEM	91.36897271	26.47448059	892.6191825	0.063931115	0.001966672	0.862886258	0.026177386	0.097579307	0.000825982	415.89761	1.026684593

Table 8. LA-ICPMS U–Pb zircon dating data of the XTL340 from the Xintianling deposit.

	Pb ppm	Th ppm	U ppm	207Pb/206Pb Ratio	207Pb/206Pb 1sigma	207Pb/235U Ratio	207Pb/235U 1sigma	206Pb/238U Ratio	206Pb/238U 1sigma	206Pb/238U Age (Ma)	206Pb/238U 1sigma
1	162.7584	1327.97	2786.917	0.061992	0.00208	0.216541	0.007261	0.025216	0.000261	160.5397	1.639684
2	112.4008	804.2761	2622.732	0.052432	0.001812	0.184311	0.00631	0.025386	0.000238	161.6042	1.494933
3	156.5895	1286.701	3143.719	0.050913	0.001425	0.181325	0.005049	0.025704	0.000236	163.6059	1.481032
4	289.9565	4001.691	2070.173	0.063124	0.001981	0.221424	0.007151	0.025267	0.000242	160.8568	1.522363
5	125.0608	983.9794	2797.928	0.04971	0.001495	0.174279	0.005068	0.025412	0.000224	161.7666	1.40774
6	162.3233	1400.659	3221.655	0.050923	0.001605	0.183729	0.00577	0.026005	0.000212	165.4973	1.329999
8	126.8413	1054.429	2488.264	0.05176	0.001811	0.186046	0.00659	0.026183	0.00036	166.6115	2.261453
9	117.7929	909.4558	2589.701	0.04697	0.001462	0.164988	0.005161	0.025367	0.000238	161.487	1.494871
10	185.7832	1665.509	3407.976	0.05224	0.001583	0.183149	0.005569	0.025345	0.000287	161.3463	1.805077
12	183.1203	1590.276	3739.657	0.04901	0.001424	0.171262	0.005023	0.025193	0.000199	160.3941	1.253843
13	172.2477	1509.76	3400.123	0.051271	0.001511	0.179143	0.00522	0.025252	0.000211	160.7609	1.326957
16	401.497	5867.655	3701.837	0.049571	0.001439	0.170975	0.004864	0.024963	0.000221	158.9448	1.389775
18	111.6549	926.5998	2144.36	0.052337	0.00177	0.183989	0.006069	0.025476	0.000214	162.1699	1.345771
Std-TEM	94.26076477	27.76954828	931.7765241	0.061328438	0.001754657	0.833390969	0.024089262	0.097708883	0.000865943	417.2342	1.910144656
Std-TEM	95.43700819	28.4993559	944.7604326	0.058840971	0.001713827	0.808673803	0.023492584	0.098886659	0.000897788	415.3452	2.294169098
Std-TEM	94.55323502	28.73544114	949.1613759	0.061328438	0.001754657	0.833390969	0.024089262	0.097708883	0.000865943	419.2334	1.560782907

The zircons in the three samples were generally 90–150- μ m in length, with a length/width ratio of 2–5. It was also found that they were colorless and transparent with some salient microcracks. Moreover, oscillatory zoning was developed in single-grain zircon, with distinct genetic characteristics of magmatic rocks. The Th/U ratios of XTL-200-01-03 and XTL-340-7 were 0.32–2.09 (mean 1.01) and 0.31–1.56 (mean 0.51). Granite porphyry was 0.37–0.63 (mean 0.52).

The testing results of the three samples in this study indicated that the zircon samples are of magmatic origin. The XTL-200-01-03 sample was fresh, medium-coarse biotite granite. The tests revealed that the weighted average $^{206}\text{Pb}/^{238}\text{U}$ age was 162.3 ± 1.2 Ma, and $\text{MSWD} = 1.3$ (18 test sites). The XTL-06 sample was a fresh granite porphyry sample, which was collected from the surface of the gold source ore block in the Xintianling mining area. The weighted average $^{206}\text{Pb}/^{238}\text{U}$ age of zircon from 18 sites was 154.3 ± 1.6 Ma, and $\text{MSWD} = 2.4$ (18 test sites). The XTL-340-7 sample was a fresh, fine-grained biotite granite sample, which was collected from the middle section 340 of the Xiaobanlong ore block in the Xintianling mining area. The weighted average $^{206}\text{Pb}/^{238}\text{U}$ age of zircon from 18 sites was estimated to be 161.8 ± 1.3 Ma, and $\text{MSWD} = 1.8$, as shown in Figures 5–8.



Figure 5. CL images of selected dated zircons from medium- and coarse-grained biotite granite. The red circles and nearby numbers indicate the spot locations and concordant ages.



Figure 6. CL images of selected dated zircons from granite porphyry. The red circles and nearby numbers indicate the spot locations and concordant ages.

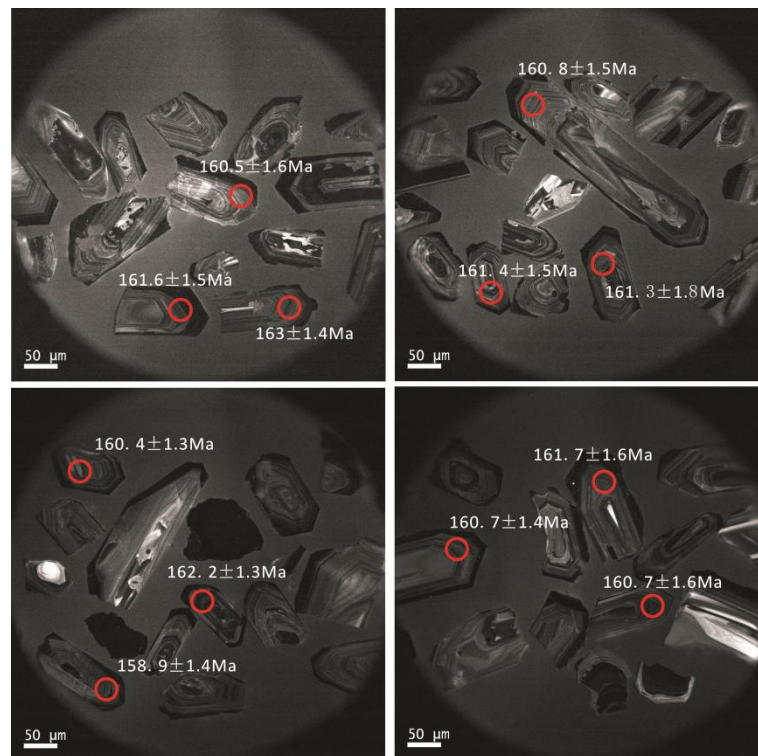


Figure 7. CL images of selected dated zircons from fine-grained biotite granite. The red circles and nearby numbers indicate the spot locations and concordant ages.

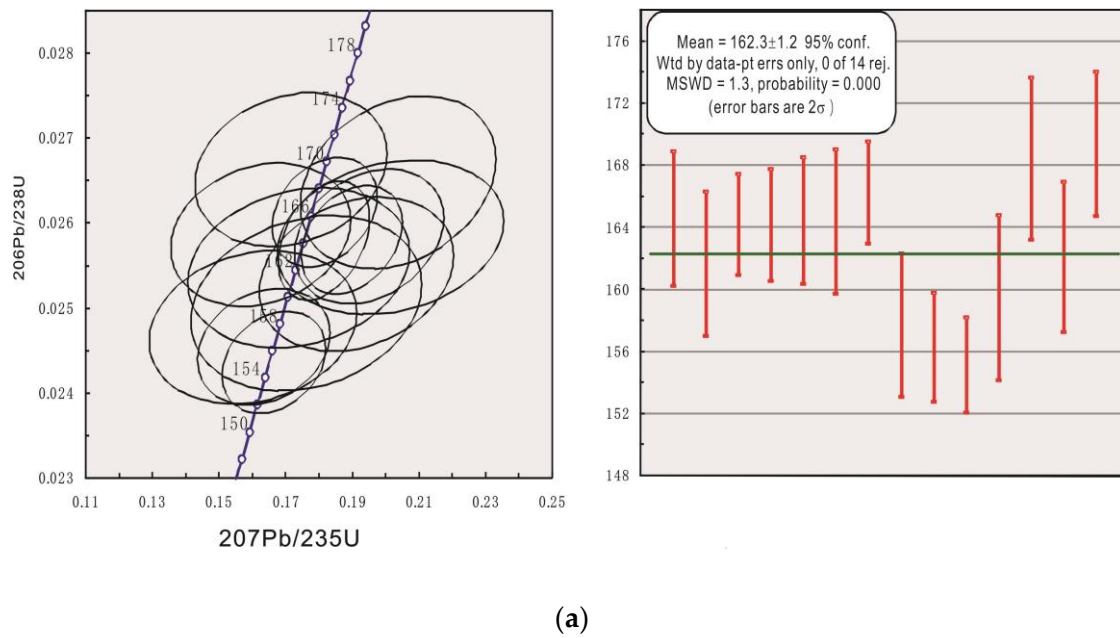


Figure 8. Cont.

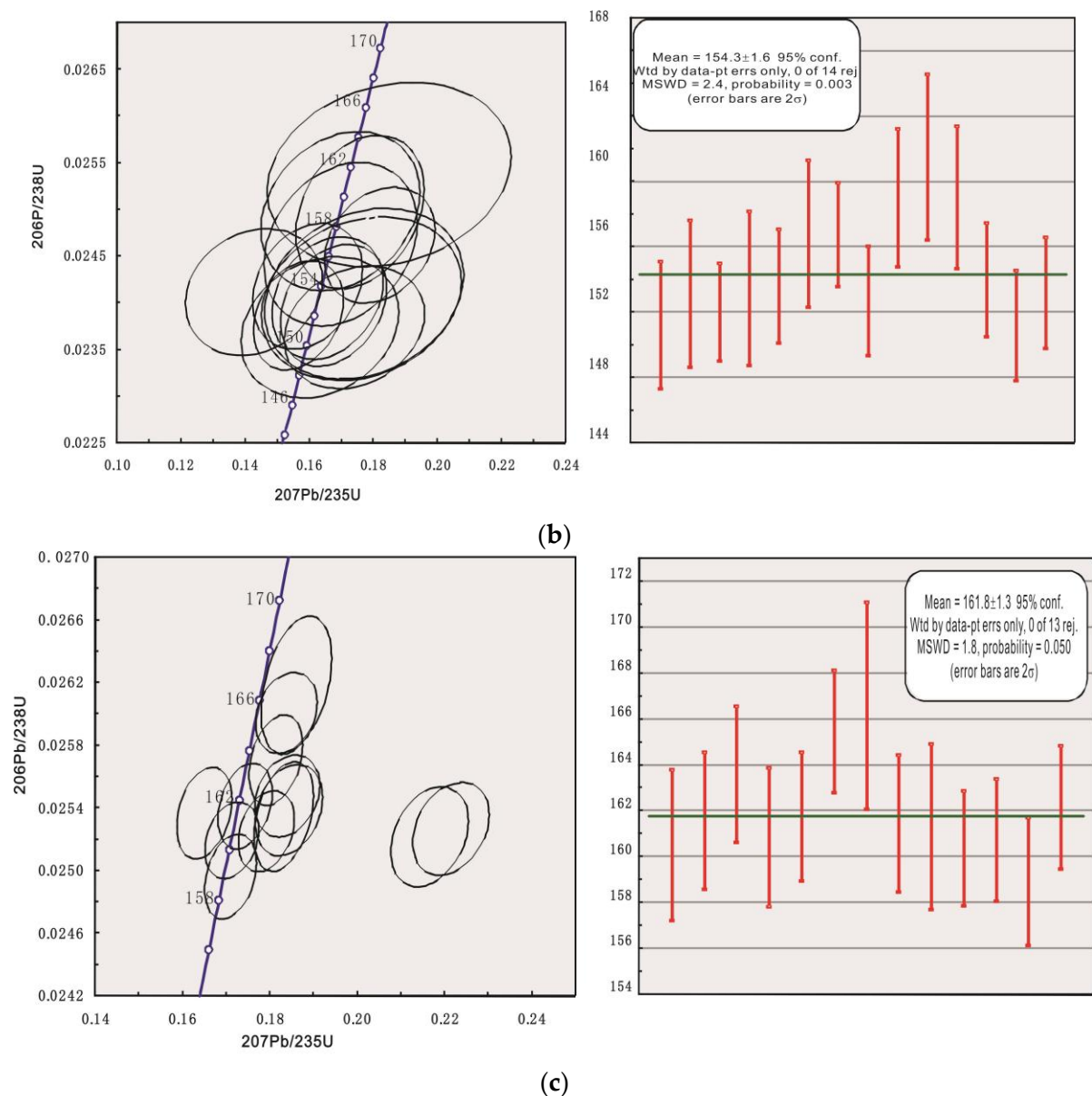


Figure 8. Zircon LA-ICP-MS U–Pb concordia diagrams for the samples XTL-200-01 (a), XTL-06 (b), XTL-340 (c).

6. Discussion

6.1. Data Analysis

The distribution of trace elements and the ratios of elements with similar geochemical characteristics are both sensitive indicators in geological processes, which allow them to be particularly useful in mineral exploration and genesis. Given their highly similar geochemical behaviors, some REEs contain useful information regarding geological evolution. Figure 9 illustrates the REEs in granite in Xintianling, which is normalized to chondrite. The REE contents indicate significant fractionation between LREEs and HREEs, with LREE/HREE ratios of 6.22 to 12.33 and $(La/Yb)_N$ ratios of 6.65 to 24.78. Delta Eu ranged from 0.09 to 0.67, with an average value of 0.52, signifying a distinct negative anomaly. In contrast, δCe (0.93 to 1.06) exhibited no conspicuous anomalies. The enrichment in LREE, the relative depletion of HREE, and a negative Eu anomaly all formed a V-type pattern (Figure 9). The consistent REE patterns indicate identical or similar sources and evolution processes. Figure 10 shows the ratio spider diagram of trace elements in the analyzed samples. The rocks depleted Ba, Ti, and Sr contents and enriched Hf and U contents. The depletion in

Ba, Ti, and Sr contents (normalized to primitive mantle) suggests that fractional crystallization was essential in their petrogenesis. Moreover, the rocks exhibited characteristics of non-orogenic granites.

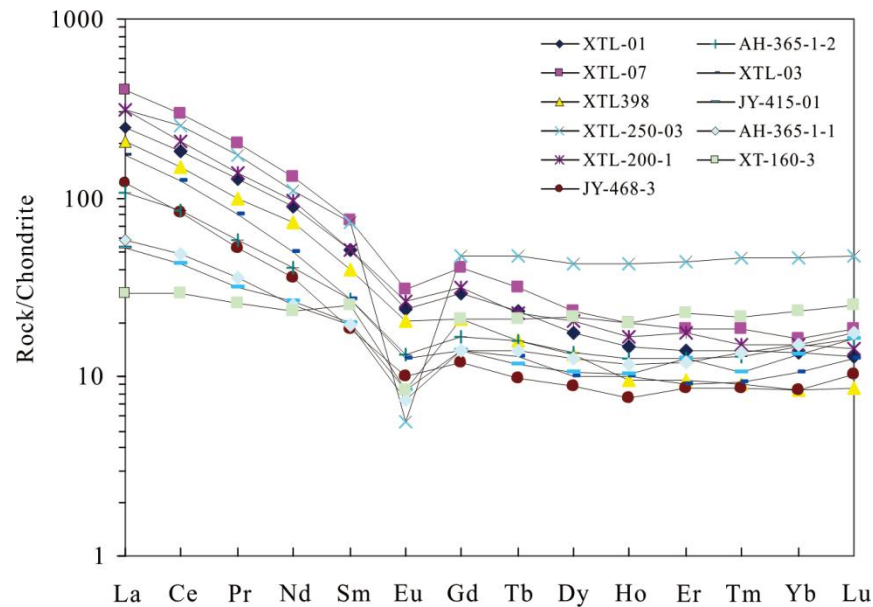


Figure 9. Chondrite-normalized REE patterns for granites in Xintianling ore field, Hunan, China.

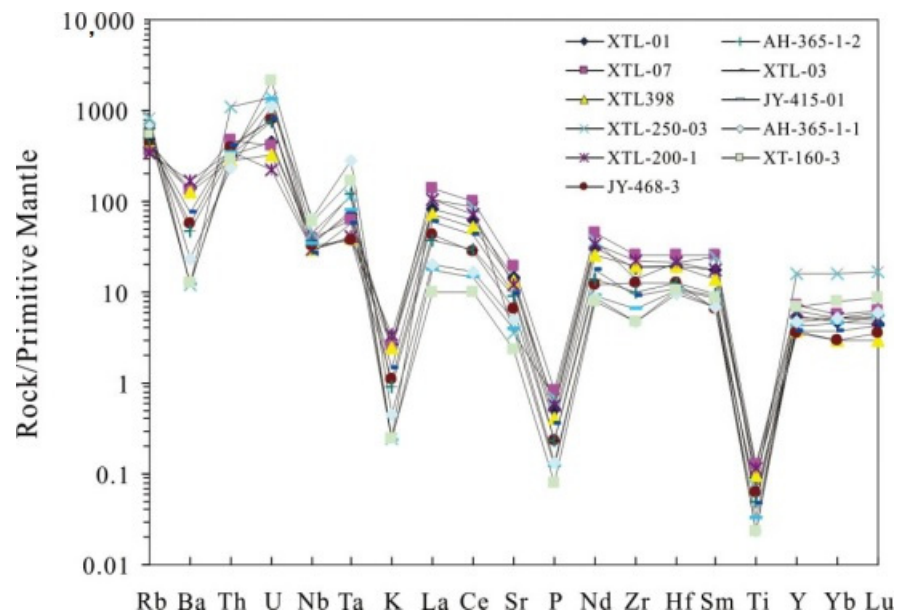


Figure 10. Primitive mantle-normalized spider diagram of trace elements for granites in Xintianling ore field, Hunan, China.

6.2. Genesis of Granite

Regionally, tin mineralization occurs mostly in the west and is related to intracontinental granite, whereas tungsten mineralization mainly occurs in the east and is related to continental margin granite. The two mineralizations are formed along with the tectonic evolution of diagenesis and the mineralization of the Nanling metallogenic belt. W-Sn metallogenic attributes, related to both intracontinental and epicontinental granite in southern Hunan, have been identified. The mineralization of tungsten and tin was previously considered to be strongly associated with Yanshanian S-type granite (such as Yaogangxian, Dengfuxian, Xihuashan, Dajishan, Tianmenshan, Hongtaoling, and Tieshanlong). Of

these types of granite, some represent transitional types, from I-type to S-type and a small amount of A-type granite. However, scholars have recently reported that many types of granite in the Nanling region are related to tin and tungsten–tin mineralization (such as Qitianling, Huashan-Guposhan, Laiziling, Jiuyishan, Xitian, Qianlishan, etc.) and represent A-type granite. In this context, Xintianling granite can be divided into three types: main-body granite, complement granite, and vein rock granite. Main granite is primarily biotite granite, and dike is primarily granite porphyry and quartz porphyry, which cuts through the early-emplaced rock mass. It is rich in aluminous biotite and formed by the anatexis of lower dry crustal materials, which are affected by the underplating or injection of mantle-derived magma, resembling S-type granite. However, the characteristics of mineral cordierite were not elucidated in this study, and the formation temperature was similar to that of granite porphyry (743 °C). Notably, our results indicated that biotite granite, related to mineralization in the Xintianling tungsten deposit, is A-type granite. (Figures 11 and 12). The following evidence of this pattern was demonstrated:

- (1) The biotite granite was rich in Si and K but poor in Mg and Ca while being peraluminous.
- (2) The biotite granite featured high Zr and Rb levels and low Sr and Ba levels. It was enriched by Rb, U, Ta, and Pb, but levels of Ba, K, Nb, La, and Ce were depleted.
- (3) In terms of REEs, light REEs enriched the granite. There was a strongly negative anomaly regarding europium, and a V-shape REE distribution pattern was formed.
- (4) The diagram of $(\text{Na}_2\text{O} + \text{K}_2\text{O})/\text{CaO} - (\text{Zr} + \text{Nb} + \text{Ce} + \text{Y})$ indicated that most of the biotite granite was in the area where A-type granite was located. Likewise, the diagram of $(\text{Na}_2\text{O} + \text{K}_2\text{O})/\text{CaO} - 10,000 \text{ Ga}/\text{AL}$ suggested that most of the biotite granite was within the area where the A-type granite was located, while a small number of samples were within the I or S-type granite location, and granite porphyry was either within or near the I or S-type granite locations.

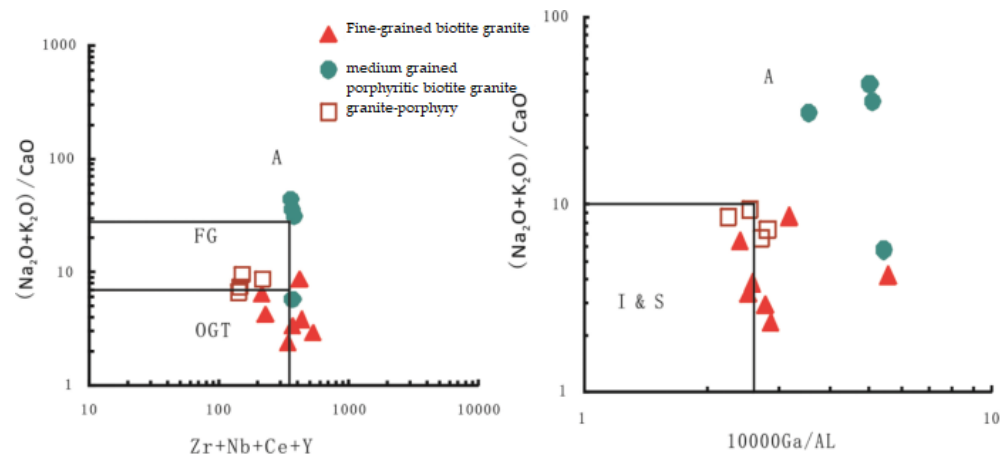


Figure 11. Plots of $(\text{Na}_2\text{O} + \text{K}_2\text{O})/\text{CaO}$ versus $(\text{Zr} + \text{Nb} + \text{Ce} + \text{Y})$ and $(\text{Na}_2\text{O} + \text{K}_2\text{O})/\text{CaO}$ versus $10,000 \text{ Ga}/\text{AL}$ of the Xintianling granite. The areas indicated in the above diagrams are from J.B. Whalen [26].

6.3. Geodynamic Settings

The geodynamic background and large-scale mineralization of tungsten and tin deposits in South China have always attracted substantial attention from geologists. Specifically, large-scale W–Sn polymetallic deposits in South China are thought to have formed catastrophically in the Yanshanian period of 160 to 150 Ma. The formation of these deposits was closely related to granite. The current understanding of the tectonic setting of the Jurassic granite in South China is the result of multiple research efforts conducted from different perspectives. One of the most controversial issues in this research field is whether the subduction of the paleo-Pacific plate occurred in South China in the early Yanshanian period or whether this was simply intraplate tectonism. Intraplate extensional

decompression or intracontinental subduction, compression, thickening, and redissolution were suggested to have occurred.

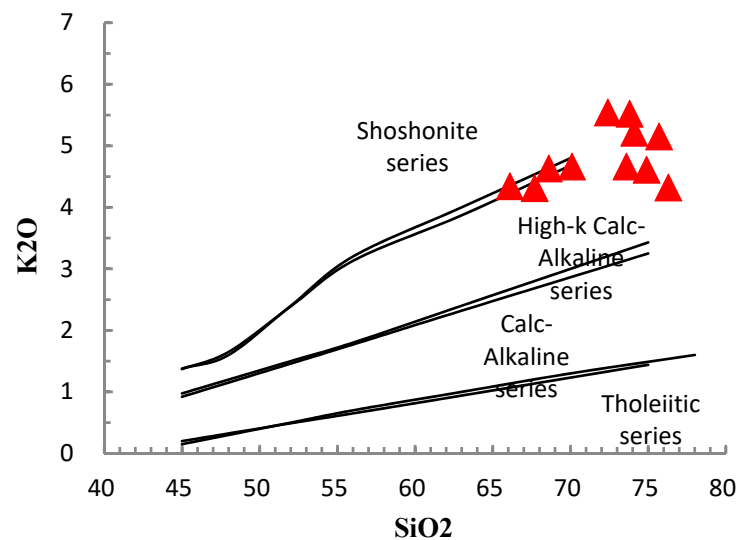


Figure 12. Granite-class diagram of $\text{SiO}_2\text{--K}_2\text{O}$ (Peccerillo [28]).

Within the literature regarding the Nanling W-Sn metallogenic belt, early scholars suggested that the belt was related to S-type granite, which was remelted by the continental crust through collision. However, the discovery of an NE-trending, alkali-rich intrusive rock belt in Qianlishan–Qitianling–Xishan–Huashan and Guposhan rock mass structures in the middle of the Nanling mountain range has created the opportunity for another working hypothesis to be researched. Other scholars have suggested that exposed granite primarily represents S-type granite. This granite was formed in a post-orogenic extensional setting, rather than through collisional compression.

There is a general relationship between types of granite and tectonic environments. Granite formed in different tectonic settings commonly exhibits distinct chemical composition, P-T conditions, and formation mechanisms. In turn, these characteristics can be used to determine the tectonic environment of granite, and they also lay the foundation for the study of regional tectonic evolution. Trace elements in rocks can be used to determine their tectonic environment. The rock trace-element ratios are plotted as $(Y + Nb) - Rb$, $(Yb + Ta) - Rb$, $Yb - Ta$, and $Y - Nb$ in Figure 13. As indicated by the tectonic environment discrimination diagram of $(Y + Nb) - Rb$, five rock samples were in the syn-COLG area; four were in the WPG area. Furthermore, Figure 13, with $(Yb + Ta) - Rb$, indicates that seven rock samples were found in the syn-COLG area, and the others were found in the WPG area. Figure 13, which illustrates $Yb - Ta$, demonstrates that most samples were in the WPG area, while Figure 13, which displays $Y - Nb$, reveals that most samples were in the VAG + syn-COLG area.

Overall, the trace-element compositions of the Xintianling intrusion suggest that it was affiliated with the Tethys-collision when the tectonic setting was transitioned from collisional orogeny/within-plate tectonism to intraplate collision orogeny.

Late Yanshanian tectonic conversion is an important driver of Xintianling magmatic activities and also provided conducive dynamic conditions for the large-scale mineralization that occurred in South China. The magmatic activities are governed by the tectonic environment. As such, their chemical compositions feature a genetic relationship with the tectonic environment. The Gd/Lu of granite ranged from 15.00 to 20.00 in extensional settings and from 8.00 to 12.00 in compressive settings. The Gd/Lu of Xintianling granite, ranging between 11.54 and 16.77, was generally higher than granite in the compressive environment. However, it was close to that of granite in the extensional environment, potentially indicating that magma intruded in extensional settings. The Nanling metallogenic belt within the main ore-forming tectonic environment is a relatively stable regional tension.

The emplacement age represents a transitional period for the tectonic environment, namely, the transition from the Indosinian orogenic to the late intraplate extensional period, which occurred in the late Yanshanian era. More specifically, the crustal deformation and magmatic activity during the Indosinian–Yanshanian period of ore-forming materials promoted the occurrence and development of mineralization, thereby creating favorable conditions for large-scale mineralization [27,28].

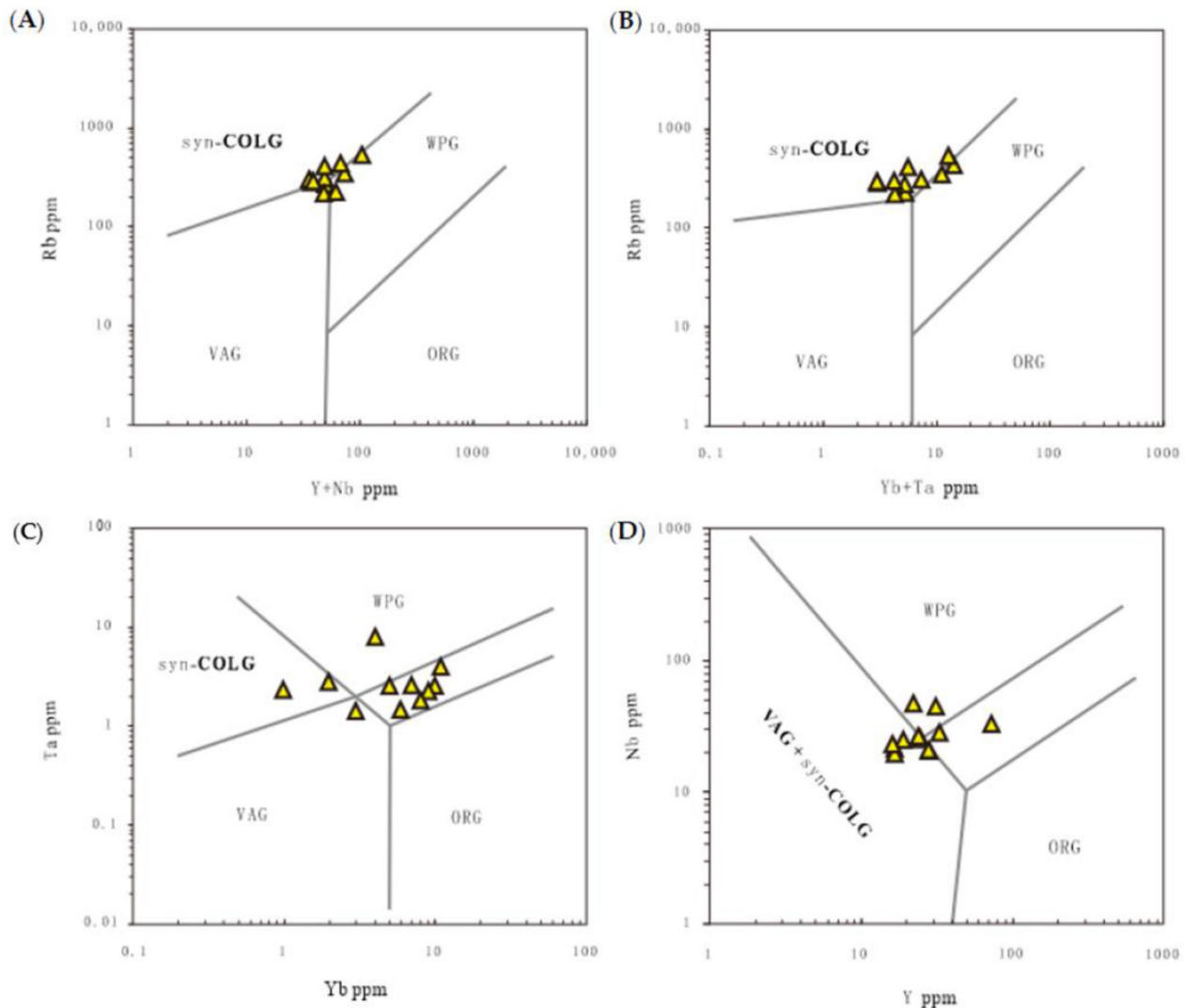


Figure 13. (A) Rb – (Y + Nb), (B) Rb – (Yb + Ta), (C) Ta – Y and (D) Nb – Y discrimination diagrams of granites (Pearce J A, [27]) VAG—volcanic arc granite; syn-COLG—syn collisional granite; WPG—within plate granite; ORG—ocean ridge granite.

7. Conclusions

This study examined the regional geological characteristics, deposit geological characteristics, and elemental geochemical characteristics of the Xintianling tungsten deposit. The analysis revealed that the deposit presented a typical skarn-type scheelite. It was the product of large-scale mineralization in Nanling in the middle–late Jurassic era (160–150 Ma). The results indicated that lithospheric extension, asthenosphere upwelling along deep faults, and intensive mantle–crust interaction processes all likely occurred under the tectonic setting in the Mesozoic era.

(1) The average SiO_2 content levels in Xintianling granite were estimated to be 72.11 wt%. $\text{K}_2\text{O} + \text{Na}_2\text{O} > 7.00\%$, i.e., the level of $w(\text{K}_2\text{O})/w(\text{Na}_2\text{O})$ was high. The Al_2O_3

content levels were generally high, with an average of 13.49 wt%. Overall, the studied granite was found to belong to the high-potassium calc-alkaline series.

(2) The fractionating degrees of light and heavy REEs were higher, and the chondrite standardized distribution pattern coincided well with these. This indicates similar magma sources and evolution histories.

(3) The evolution of granite intrusions was affected by crust–mantle interaction, which supplied the material source.

(4) The rock was likely to have formed from partial melting by means of crust–mantle interactions in the period of the collision orogeny and intraplate. This pattern was peculiarly prominent during the conversion period of both in the tensile tectonic environment.

(5) LA-ICP-MS zircon U-Pb dating indicated the middle–coarse biotite granite (162.3 ± 1.2 Ma, MSWD = 1.3), the fine-grained biotite granite (161.8 ± 1.3 Ma, MSWD = 1.8), and the granite porphyry (154.3 ± 1.6 Ma, MSWD = 2.4) were formed in the late Jurassic period. The scheelite was revealed to have an Sm-Nd isochron age of 157.1 ± 3.2 , which is within the margin of error of molybdenite's Re-Os isochron age of 159.1 ± 2.6 Ma. Both ages agreed well with the zircon U-Pb ages, thus suggesting that the formation of the Xintianling scheelite deposit was synchronous with the development of granite intrusions and that ore-forming fluids were derived from these intrusions.

Author Contributions: Conceptualization, W.Y.; methodology, W.Y.; software, M.Z.; formal analysis, W.Y.; investigation, M.Z. and W.Y.; data curation, J.Y.; writing—original draft preparation, W.Y.; writing—review and editing, X.C. and W.Y.; visualization, J.Y.; supervision, J.Y. All authors have read and agreed to the published version of the manuscript.

Funding: This research was supported by the Major Research plan of National Science Foundation of China [92062106], the Science and Technology Support Plan of Guizhou Province [Qian (2017)1078] and Qian (2019)1138], the High-level talent introduction program for the Guizhou Institute of Technology (0203001018040).

Institutional Review Board Statement: Not applicable.

Informed Consent Statement: Not applicable.

Data Availability Statement: Not applicable.

Conflicts of Interest: The authors declare no conflict of interest.

References

1. Fan, W. Origin of the Qitianling granite in southern Hunan: Rb-Sr isotopic and REE constraints. *Geotecton. Metallog.* **1987**, *11*, 47–54.
2. Zhu, J.C. On the emplacement age and material sources for the granites of Cailing supemnit Qitianling pluton, south Hunan Povince. *Geol. Rev.* **2003**, *49*, 245–252.
3. Deng, X.G.; Li, X.H.; Liu, Y.M.; Huang, G.F.; Hou, M.S. Geochemical characteristics of Qitianling granites and their implications for mineralization. *Acta Petmlogicaet Mineral.* **2005**, *24*, 93–102.
4. Liu, Y.S.; Hu, Z.C.; Zong, K.Q.; Gao, C.G.; Gao, S.; Xu, J.; Chen, H.H. Reappraisal and refinement of zircon U-Pb isotope and trace element analyses by LA-ICP-MS. *Chin. Sci. Bull.* **2010**, *5*, 1535–1546. [[CrossRef](#)]
5. Peng, J.T.; Zhou, M.F.; Hu, R.Z.; Shen, N.P.; Yuan, S.D.; Bi, X.W.; Du, A.D.; Qu, W.J. Precise molybdenite Re-Os and mica Ar-Ar dating of the Mesozoic Yaogangxian tungsten deposit, central Nanling district, South China. *Miner. Depos.* **2006**, *41*, 661–669. [[CrossRef](#)]
6. Deng, S.H.; Xu, H.C.; Liu, Y.S. Relationship between Tectonic Setting and Mineral Assemblages in Qianlishan-Qitianling Mineralized Concentration Area. *Geol. Miner. Resour. South China* **2003**, *51*–55.
7. Cai, M.H.; Han, F.B.; He, L.Q.; Liu, G.Q.; Chen, K.X.; Fu, J. He, Ar isotope characteristics and Rb-Sr dating of the Xintianling skarn scheelite deposit in southern Hunan, China. *Acta Geosci. Sin.* **2008**, *29*, 167–173.
8. Zhang, R.; Lu, J.; Huang, X.; Zhang, Q.; Zhao, X.; Li, X. Formation of the Xintianling scheelite skarn deposit, Nanling Range, South China: Insights from petrology, mineral chemistry and C-H-O-S-Pb isotopes: Formation of the Xintianling scheelite skarn deposit, Nanling Range, South China: Insights from petrology, mineral chemistry and C-H-O-S-Pb isotopes. *Geol. Appl. Miner. Depos. Sga* **2019**, 186–189.
9. Li, H.L.; Bi, X.W.; Hu, R.Z.; Peng, J.T.; Shuang, Y.; Li, Z.L.; Li, X.M.; Yuan, S.D. Mineral chemistry of biotite in the Qitianling granite associated with the Furong tin deposit: Tracing tin mineralization signatures. *Acta Petrol. Sin.* **2007**, *23*, 2605–2614. (In Chinese with English Abstract)

10. Jiang, Y.H.; Jiang, S.Y.; Zhao, K.D.; Ling, H.F. Petrogenesis of Late Jurassic Qianlishan granites and mafic dykes, Southeast China: Implications for a back-arc extension setting. *Geol. Mag.* **2006**, *143*, 457–474. [[CrossRef](#)]
11. Bai, D.Y.; Chen, J.C.; Ma, T.Q.; Wang, X.H. Geochemical characteristics and tectonic setting of Qitianling A-type granitic pluton in southeast Hunan. *Acta Petrol. Mineral.* **2005**, *24*, 255–272, (In Chinese with English Abstract).
12. Rudnick, R.L.; Fountain, D.M. Nature and composition of the continental crust: A lower crustal perspective. *Rev. Geophys.* **1995**, *33*, 267–309. [[CrossRef](#)]
13. Li, X.H.; Qi, C.S.; Liu, Y.; Liang, X.R.; Tu, X.L.; Xie, L.W.; Yang, Y.H. Petrogenesis of the Neoproterozoic bimodal volcanic rocks along the western margin of the Yangtze Block: New constraints from Hf isotopes and Fe/Mn ratios. *Chin. Sci. Bull.* **2005**, *50*, 2481–2486. [[CrossRef](#)]
14. Li, X.H. Geochemistry of the Longsheng Ophiolite from the southern margin of Yangtze Craton, SE China. *Geochem. J.* **1997**, *31*, 323–337. [[CrossRef](#)]
15. King, P.L.; White, A.J.R.; Chappell, B.W. Characterization and origin of aluminous. A type granites of the Lachlan Fold Belt, southeastern Australia. *J. Petrol.* **1997**, *36*, 371–391. [[CrossRef](#)]
16. Cai, M.; Liang, T.; Wu, D. Geochemical characteristics of granites and its structural genetic environment in the Nandan hechi metallogenic belt, northwest Guangxi. *Geotecton. Metallog.* **2004**, *28*, 306–313.
17. Mao, J.W.; Cheng, Y.B.; Chen, M.H.; Franco, P. Major types and time–space distribution of Mesozoic ore deposits in South China and their geodynamic settings. *Miner. Depos.* **2013**, *48*, 267–294.
18. Sakoma, E.M.; Martin, R.F.; Williams-Jones, A.E. The late stages of evolution of the Kwadonkaya A-type granite complex, Nigeria, as deduced from mafic minerals. *J. Afr. Earth Sci.* **2000**, *30*, 329–350. [[CrossRef](#)]
19. Irvine, T.H.; Baragar, W.R.A. A guide to the chemical classification of the common volcanic rocks. *Can. J. Earth Sci.* **1971**, *8*, 523–548. [[CrossRef](#)]
20. Sun, S.S.; McDonough, W.F. Chemical and isotopic systematics of oceanic basalts: Implications for mantle composition and processes. In *Magmatism in Ocean Basins*; Saunders, A.D., Norry, M.J., Eds.; Geological Society of London: London, UK, 1989; Volume 42, pp. 313–345.
21. Whalen, J.B.; Currie, K.L.; Chappell, B.W. A-type granites: Geochemical characteristics, discrimination and petrogenesis. *Contrib. Mineral. Petrol.* **1987**, *95*, 407–419. [[CrossRef](#)]
22. Rubatto, D. Zircon trace element geochemistry: Distribution coefficients and the link between U-Pb ages and metamorphism. *Chem. Geol.* **2002**, *184*, 123–138. [[CrossRef](#)]
23. Corfu, F.; Hanchar, J.M.; Hoskin, P.W.; Kinny, P. Atlas of zircon textures. *Rev. Mineral. Geochem.* **2003**, *53*, 469–500. [[CrossRef](#)]
24. Rubatto, D. Zircon: The Metamorphic Mineral. *Rev. Mineral. Geochem.* **2017**, *83*, 261–295. [[CrossRef](#)]
25. Fornelli, A.; Micheletti, F.; Piccarreta, G. Late-Proterozoic to Paleozoic history of the peri-Gondwana Calabria–Peloritani Terrane inferred from a review of zircon chronology. *SpringerPlus* **2016**, *5*, 1–19. [[CrossRef](#)] [[PubMed](#)]
26. Fornelli, A.; Festa, V.; Micheletti, F.; Spiess, R.; Tursi, F. Building an Orogen: Review of U-Pb Zircon Ages from the Calabria–Peloritani Terrane to Constrain the Timing of the Southern Variscan Belt. *Minerals* **2020**, *10*, 944. [[CrossRef](#)]
27. Pearce, J.A.; Harris NB, W.; Tindle, A.G. Trace element discrimination diagrams for the tectonic interpretation of granitic rocks. *Petrology* **1984**, *25*, 956–983. [[CrossRef](#)]
28. Peccerillo, R.; Taylor, S.R. Geochemistry of Eocene Calc-Alkaline Volcanic Rocks from the Kastamonu Area, Northern Turkey. *Contrib. Mineral. Petrol.* **1976**, *58*, 63–81. [[CrossRef](#)]